Atmos. Meas. Tech., 15, 4473–4487, 2022
https://doi.org/10.5194/amt-15-4473-2022


Atmospheric Measurement Techniques
Open Access
EGU

# Development of a broadband cavity-enhanced absorption spectrometer for simultaneous measurements of ambient $NO_3$, $NO_2$, and $H_2O$

**Woohui Nam[1], Changmin Cho[1], Begie Perdigones[1], Tae Siek Rhee[2], and Kyung-Eun Min[1]**

[1]School of Earth Sciences and Environmental Engineering, Gwangju Institute of Science and Technology (GIST), 123 Cheomdangwagi-ro, Buk-gu, Gwangju 61005, South Korea
[2]Korea Polar Research Institute, 26 Songdomirae-ro, Yeonsu-gu, Incheon 21990, South Korea

**Correspondence:** Kyung-Eun Min (kemin@gist.ac.kr)

Received: 4 April 2022 – Discussion started: 11 April 2022
Revised: 14 June 2022 – Accepted: 23 June 2022 – Published: 3 August 2022

**Abstract.** We describe the characteristics and performances of our newly built broadband cavity-enhanced absorption spectrometer for measurements of nitrate radical ($NO_3$), nitrogen dioxide ($NO_2$), and water vapor ($H_2O$). A customized vibration-resistance cavity layout incorporated with $N_2$ purging on high-reflection mirror surfaces was implemented with a red light-emitting diode (LED) as a light source. In general, this system achieved over 40 km (up to 101.5 km) of effective light path length at 662 nm from a 0.52 m long cavity. For accurate $NO_3$ measurement, the measured absorption spectrum of $H_2O$ was used for simultaneous concentration retrievals with the other species instead of being treated as interferences to be removed or corrected prior to $NO_3$ detection. Synthesized $N_2O_5$ crystals under atmospheric pressure were used for performance tests of linear response and transmission efficiency. From the standard injection experiments of $NO_3$, $NO_2$, and $H_2O$, high linearities were observed ($R^2 \geq 0.9918$). The total $NO_3$ transmission efficiency through the system was determined to be 81.2 % ($\pm$2.9, 1$\sigma$) within the residence time of 2.59 s. The precisions (1$\sigma$) of $NO_3$, $NO_2$, and $H_2O$ in 1 Hz measurement from a single pixel on the charge-coupled device (CCD) were 1.41 pptv, 6.92 ppbv, and 35.0 ppmv with uncertainties of 10.8 %, 5.2 %, and $\geq$ 20.5 %, respectively, mainly from the errors in the literature absorption cross-section. The instrument was successfully deployed aboard the Korean icebreaker R/V *Araon* for an expedition conducted in the remote marine boundary layer in the Arctic Ocean during the summer of 2021.

## 1 Introduction

The nitrate radical ($NO_3$) has drawn considerable attention due to its significant influence on nocturnal nitrogen oxide chemistry after the first observation in the troposphere (Noxon et al., 1980; Platt et al., 1980; Brown and Stutz, 2012). $NO_3$ is mainly produced from the oxidation of nitrogen dioxide ($NO_2$) by ozone ($O_3$, Reaction R1) and is in thermal equilibrium with dinitrogen pentoxide ($N_2O_5$) from its further combination reaction with $NO_2$ (Reaction R2).

The role of $NO_3$ as an oxidant especially for the unsaturated volatile organic compounds (VOCs) becomes more critical at night not only because of its extremely low abundance due to the losses by rapid photolysis (Reaction R3; Stark et al., 2007) and reaction with NO (Reaction R4) but also because of the negligible amount of photochemically induced hydroxyl radical. Particularly, alkenes with more than two double bonds from biogenic sources (e.g., isoprene and terpenes; Winer et al., 1984; Ng et al., 2017) and reduced sulfur compounds like dimethylsulfide (DMS; Allan et al., 2000) are susceptible to be oxidized by $NO_3$ (Reaction R5).

$$NO_2 + O_3 \rightarrow NO_3 + O_2 \quad \text{(R1)}$$

$$NO_3 + NO_2 + M \leftrightarrow N_2O_5 + M \quad \text{(R2)}$$

$$NO_3 + h\upsilon \rightarrow NO_2 + O(^3P) (< 587\,\text{nm})$$

$$NO_3 + h\upsilon \rightarrow NO + O_2 (< 714\,\text{nm}) \quad \text{(R3)}$$

$$NO_3 + NO \rightarrow 2NO_2 \quad \text{(R4)}$$

$$NO_3 + \text{alkenes, aromatics, DMS} \rightarrow \text{product} \quad \text{(R5)}$$

$$N_2O_{5(g)} + (H_2O_{(aq)} \text{ and/or } Cl^-{}_{(aq)}) \rightarrow (2-\varphi)NO^-{}_{3(aq)} + \varphi ClNO_{2(g)}, (0 \le \varphi \le 1) \quad \text{(R6)}$$

As shown in Reaction (R6), $N_2O_5$, a reservoir species of $NO_3$, can undergo heterogeneous reaction to form gaseous nitryl chloride ($ClNO_2$) and/or aqueous nitrate (Roberts et al., 2008). This uptake on aerosol can act as a dominant nitrate formation path under haze events (Chang et al., 2018; McDuffie et al., 2019; Lin et al., 2020; Liu et al., 2020). Meanwhile, $ClNO_2$ can be photolyzed to $NO_2$ and Cl radical after following sunrise; consequently, it not only conserves $NO_x$ (=NO + $NO_2$) but also accelerates oxidation speed by adding the Cl radical into the atmosphere (Osthoff et al., 2008; Le Breton et al., 2018).

In addition, the important roles of daytime $NO_3$ and $N_2O_5$ have been reported in terms of their contributions to VOC oxidation and aerosol evolution (Geyer, 2003; Brown et al., 2005, 2016, 2017; Osthoff et al., 2006; Wang et al., 2014; Wang et al., 2020; Foulds et al., 2021). Brown et al. (2017) observed a non-negligible amount of $N_2O_5$ (up to 35 pptv) during the daytime under high $NO_x$ conditions, and Foulds et al. (2021) found competitive $NO_3$ loss by VOC oxidation with photolysis, even in daytime. These findings indicate that the impacts of $NO_3$-driven chemistry are not limited to nighttime.

Because of high reactivity and thus short lifetime and low mixing ratio (a few to several parts per trillion by volume), observation of the ambient $NO_3$ is challenging. To our best knowledge, no commercial instruments are available at present, and only a few in situ measurement techniques have been used. Systems based on laser-induced fluorescence (LIF; Wood et al., 2003; Matsumoto et al., 2005) and matrix isolation electron spin resonance (MIESR; Mihelcic et al., 1993) have been reported. However, most of the contemporary instruments in active use even in intercomparison work (Dorn et al., 2013) are based on absorption spectroscopic techniques capturing the strong $B^2E'$–$X^2A'_2$ electronic transition of $NO_3$ at 662 nm (Yokelson et al., 1994). Differential optical absorption spectroscopy (DOAS), characterized by a long physical path length, has been widely used for several decades (Platt et al., 1980; Heintz et al., 1996; Allan et al., 1999; Geyer et al., 2001b; McLaren et al., 2004; Stutz et al., 2004; Vrekoussis et al., 2004; Li et al., 2007; Sommariva et al., 2007; Asaf et al., 2009; Wang et al., 2013; Lu et al., 2016). Meanwhile, more compact instruments with an optical cavity have been recently developed for $NO_3$ measurements; cavity ring-down spectroscopy (CRDS; King et al., 2000; Brown et al., 2001; Simpson, 2003; Ayers et al., 2005; Nakayama et al., 2008; Schuster et al., 2009; Flemmer and Ham, 2012; Hu et al., 2014; Wang et al., 2015; Li et al., 2018; Wu et al., 2020) and cavity-enhanced absorption spectroscopy (CEAS) are the most representative techniques. In particular, CEAS instruments with broadband light sources for $NO_3$ measurement were developed for field (Langridge et al., 2008; Varma et al., 2009; Kennedy et al., 2011; Wang et al., 2017; Suhail et al., 2019; Wang and Lu, 2019) and laboratory studies (Venables et al., 2006; Wu et al., 2014; Fouqueau et al., 2020) with the advantages of a capability for simultaneous measurements of multiple species and the applicability of cheap light sources (e.g., light-emitting diode (LED), arc Xe lamp, and supercontinuum radiation source).

One of the main difficulties for accurate $NO_3$ measurement by CEAS is $H_2O$ treatment. Due to the strong but narrow absorption by $H_2O$ around 660 nm (Ball and Jones, 2003), the contribution of $H_2O$ on light extinction needs to be well characterized. Several methods such as a look-up table (Langridge et al., 2008; Varma et al., 2009; Suhail et al., 2019), iterative calculation (Kennedy et al., 2011), and frequent $NO_3$ zeroing via NO titration (Wang et al., 2017) were adopted to overcome this issue.

Based on the capability of species-specific absorption cross-section measurements by CEAS (Axson et al., 2011; Chen and Venables, 2011; Young et al., 2011, 2014; Kahan et al., 2012; Sheps, 2013; Thalman and Volkamer, 2013; Prakash et al., 2018; He et al., 2021; Wang et al., 2022), we suggest a new approach using measured $H_2O$ spectrum for the simultaneous quantification of $NO_3$, $NO_2$, and $H_2O$, which is simple and efficient enough for atmospheric application. Through this paper, we present not only our newly built broadband cavity-enhanced absorption spectrometer (BBCEAS) with detailed descriptions of design and performances but also linearity test results with $H_2O$ in atmospherically relevant ranges. Moreover, we also show the results of the shipborne measurement of $NO_3$ in the Arctic Ocean, indicating successful performance of the instrument in field application.

## 2 Instrumental setup

BBCEAS is a sensitive instrument to directly measure the abundance of a target species and/or its optical extinction properties, introduced by Fiedler et al. (2003). Details on the working principle can be found in Ball and Jones (2003) as well as Gagliardi and Loock (2014). Briefly, this technique is based on the measurement of light extinctions in a relatively broad wavelength range. A system based on this method basically consists of a broadband light source, a high-finesse optical cavity formed by a pair of high-reflection (HR) mirrors, and detector(s). The light from the source resonates inside the cavity and rapidly reaches a steady state with the wavelength-specific attenuated intensity through the loss processes of (1) transmission, diffraction, and absorption by HR mirrors, (2) scattering by particles and gases (i.e., Mie and Rayleigh scattering), and (3) absorption by sampled trace

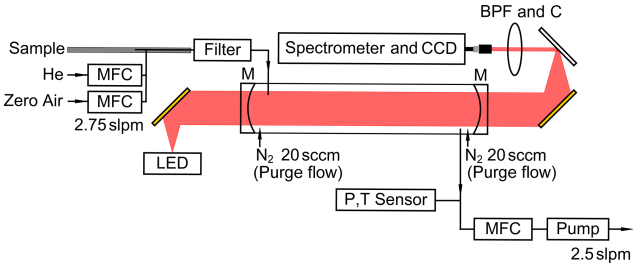


**Figure 1.** Schematic of the $NO_3$ BBCEAS system with light path (shaded in red) and gas flows (black arrows). High-reflection mirrors (M), band-pass filter (BPF), fiber collimator (C), mass flow controllers (MFCs), and sensors of precision pressure transducer (P) and thermocouple (T) are marked.

gases in the cavity. The transmitted light from the cavity is then detected by the spectrometer and charge-coupled device (CCD) or photodiode array to monitor the light extinction spectrum.

The schematic diagram of our single-channel BBCEAS is shown in Fig. 1. The material, dimensions, and design of the novel cage system on optical mounts for stable performance with respect to vibration and pressure changes during the field deployment were adopted from the glyoxal (CHOCHO) and nitrous acid (HONO) instrument described in Min et al. (2016). Detailed descriptions of the optical layout, flow system, and data acquisition system are given in the following section.

### 2.1 Optical layout

An LED (LZ1-10R202-0000, LedEngin, Germany) centered at 660 nm is used as a broadband light source and is mounted on a home-built module with copper plate, thermoelectric cooler, heat sink, XYZ translator (LP-1A-XYZ, Newport Corp., USA), and fan to control the position and temperature ($20 \pm 0.1$ °C) precisely. The light from the LED is collimated by an off-axis parabolic mirror (50328AU, Newport Corp., USA) and enters the cavity. The HR mirrors (FiveNine Optics, USA) for high-finesse optical cavity are mounted at a distance of 51.5 cm occupied by a Teflon cell (1 in. outer diameter (o.d.) and 1 mm thickness). The light exiting the cavity is then focused by another parabolic mirror (50331AU, Newport Corp., USA), filtered through a colored band-pass filter ($660 \pm 5$ nm, FB-660-10, Thorlabs Inc., USA) and coupled to a fiber collimator (74-UV, Ocean Optics Inc., USA). The customized optic fiber (Seokwang Optical Co., Korea) with linearly assembled seven 200 µm diameter cores is aligned along the slit axis of the spectrometer (HRS-300MS-NI, Princeton Instruments Inc., USA).

Light is then transmitted to a diffraction grating ($1200\,\mathrm{G\,mm^{-1}}$, 750 nm blaze, 68 mm × 68 mm) and dispersed with respect to its wavelength. A CCD is used as a detector (PIXIS-2KX, Princeton Instruments Inc., USA) to monitor the spectra of the final transmitted light intensity and is cooled to −70 °C to minimize the dark current. The wavelength coverage from 632 to 691 nm and the spectral resolution of 0.47 nm as full width at half maximum (FHWM) were calibrated with the narrow Ne emission lines (NE-2, Ocean Optics Inc., USA). The entire optical layout was housed in a temperature-controlled optic box to maintain constant performances regardless of environmental changes.

The overall configuration of the optics is similar to the system described by Min et al. (2016); however, the main difference is that we have an independent cavity for an individual channel rather than two channels sharing one parabolic mirror plate. This modification minimizes potential interferences of light leaking from the adjacent cell and provides convenience in operation and maintenance aspects (i.e., HR mirror cleaning and LED swapping).

### 2.2 Flow and data acquisition system

The air sample is drawn into perfluoroalkoxy alkene (PFA) inlet tubing with a constant flow rate of 2.5 slpm (standard liter per minute) by a mass flow controller (Alicat Scientific, USA) and a scroll pump (IDP-3, Agilent Technologies Inc., USA). The design of the coaxial inlet following Min et al. (2016) is used to minimize the pressure change during the mirror reflectivity measurements and sampling cycles (see Sect. 3.1.1). On the downstream of the inlet, a 2 µm polytetrafluoroethylene (PTFE) membrane filter (R2PJ047, Pall Corporation, USA) is used to minimize the light extinction owing to Mie scattering by sampled aerosols in the cavity as well as to prevent reflectivity degradation of HR mirrors. The air then passes through 1/16 in. inner diameter (i.d.) PFA tubing into the cavity to minimize $NO_3$ loss by shortening the residence time with the scheme of reduced pressure operation as in Fuchs et al. (2008). The temperature and pressure inside the cavity are measured at the outflow of the cell.

Another difference with the cavity system in Min et al. (2016) is the addition of a purging system. As an active strategy to prevent sampled air contact on the HR mirror surface, ultra-high-purity (UHP) $N_2$ flows (> 99.999 %, 20 standard cubic centimeter per minute, sccm) are introduced on each side of the cavity mirrors via custom-designed PFA cell flanges with orifices (50 µm, SS-1/8-Tube-50, Lenox Laser, USA). The effect of purge flow on the volume occupied by the air sample in the cavity was estimated as in Sect. 3.1.2.

Our instrument is operated and controlled automatically with the customized software programmed by LabView (National Instruments) for flow rates and temperatures of LED and CCD. The transmitted light spectra and other auxiliary data including temperatures, pressures, and flow rates for the extinction spectrum calculation are acquired via this program as well.

## 3 Characterization

From the spectrum of measured light extinction inside the cavity, $\alpha(\lambda)$, the number density ($x_i$) of species $i$ can be calculated from Eq. (1).

$$\alpha(\lambda) = \sum T_i \sigma_i(\lambda) x_i + \alpha_{\text{Mie}} + \alpha_{\text{Rayleigh}} = \left(\frac{1 - R(\lambda)}{d_{\text{eff}}}\right)\left(\frac{I_{\text{out},0}(\lambda)}{I_{\text{out}}(\lambda)} - 1\right) \quad (1)$$

Here, $T_i$ is the transmission efficiency from the inlet to the cavity, $\sigma_i$ corresponds to the absorption cross-section, $R$ stands for mirror reflectivity, and $d_{\text{eff}}$ is effective cavity length. The $\alpha_{\text{Rayleigh}}$ and $\alpha_{\text{Mie}}$ refer to the optical extinctions due to Rayleigh and Mie scattering, while we neglect $\alpha_{\text{Mie}}$ owing to the aerosol filter on the inlet airway. The intensities of light transmitted from the cavity with and without the absorbing species are symbolized as $I_{\text{out}}$ and $I_{\text{out},0}$, respectively. Here, we define $I_{\text{out},0}$ as the light intensity when the cavity is filled with dry zero air (ZA) only. Thus, for the accurate quantification of $x_i$ based on Eq. (1), not only the reference spectrum $\sigma_i$ but also the instrumental parameters such as $d_{\text{eff}}$, $R$, $I_{\text{out},0}$, and $T_i$ should be characterized beforehand.

### 3.1 Determination of cavity parameters

#### 3.1.1 Mirror reflectivity, $R(\lambda)$

$R(\lambda)$ can be derived from the well-known Rayleigh scattering differences in two species, and we selected helium (He) and ZA as shown in Eq. (2). For our instrument, a 2.75 slpm flow of He or ZA (99.999 % each, Daedeok Gas Co. Ltd.) is overflowed into coaxial inlet tubing so that 2.5 slpm flow is introduced into the cavity, the same as the flow rate of the sample, while the rest of the flow is streamed towards the outside of the inlet to minimize the pressure change inside the cavity.

$$R(\lambda) = 1 - d \left[\frac{I_{\text{ZA}}(\lambda)\alpha_{\text{Rayleigh,ZA}}(\lambda) - I_{\text{He}}(\lambda)\alpha_{\text{Rayleigh,He}}(\lambda)}{I_{\text{He}}(\lambda) - I_{\text{ZA}}(\lambda)}\right] = 1 - \frac{d}{L_{\text{Light}}(\lambda)} \quad (2)$$

In Eq. (2), $I_i$ refers to the transmitted spectral intensity filled with gas species $i$. $L_{\text{Light}}$ is the theoretically calculated effective light path length under the assumption that light attenuation is solely driven by the mirror and the cavity length, $d$. The $\alpha_{\text{Rayleigh,i}}$ was calculated from the literature Rayleigh scattering cross-sections of $N_2$ (Bodhaine et al., 1999), $O_2$, and He (Shardanand and Rao, 1977) considering pressure and temperature changes.

Figure 2 shows the cavity characteristics such as the $I_{\text{ZA}}(\lambda)$, $I_{\text{He}}(\lambda)$, $R(\lambda)$, and $L_{\text{Light}}(\lambda)$ as examples acquired during the $T_{\text{E,NO}_3}$ quantification experiments (described in Sect. 3.3.2). Although the difference of the transmitted light intensities between He and ZA injections was largest near 662 nm (Fig. 2a), the wavelength corresponding to the highest $R(\lambda)$ value was shifted to 672.5 nm due to the incorporated wavelength-dependent characteristics of Rayleigh scattering and mirror reflectivity (Fig. 2b). $L_{\text{Light}}$ exceeded 98 km (Fig. 2c) within the wavelength range for fitting (shaded in light red in Fig. 2). Especially at 662 nm, where $NO_3$ absorption peaks, $R$ and $L_{\text{Light}}$ were 99.9995 % and 101.5 km, which are superior values to other reported ones from previous BBCEAS studies (Table 1 in Sect. 3.5). The uncertainty for $R(\lambda)$ estimation is 2.2 %, mainly from an error in the Rayleigh scattering spectrum of ZA (2 %; Washenfelder et al., 2008) and rarely from the temperature and pressure measurements (0.7 % and 0.5 %, respectively).

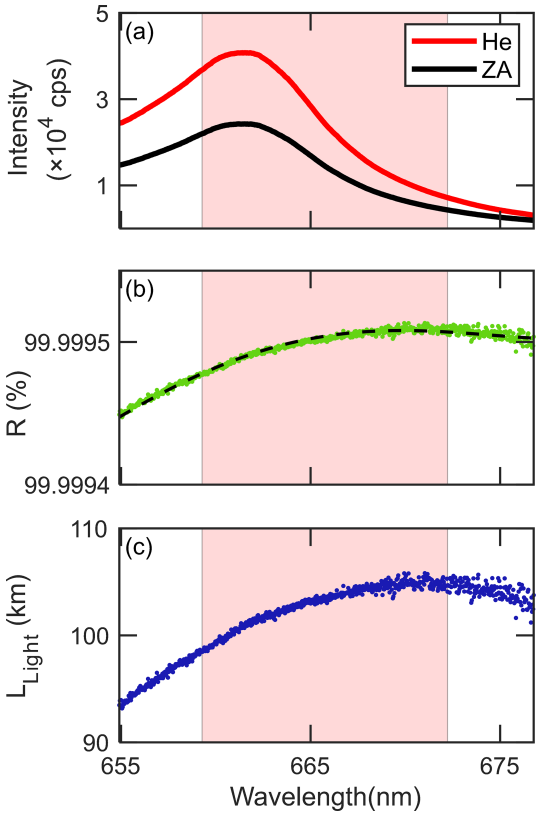


**Figure 2.** Cavity characteristics of 1 min averaged **(a)** transmitted light intensities with zero air (ZA) and He injection, **(b)** mirror reflectivity, $R$ (dashed black line is fitted with fourth-order polynomial), and **(c)** effective light path length, $L_{\text{Light}}$. Shaded area in light red represents fitted range for the number density retrieval.

#### 3.1.2 Effective cavity length, $d_{\text{eff}}$

The volume occupied by the sample in the cavity should be accurately evaluated. Due to the reduction in the sample volume by addition of the purge flow, the $d_{\text{eff}}$ differs from both the cavity length defined by mirror separation (51.5 cm)

**Table 1.** Comparison of BBCEAS performances for $NO_3$ measurement.

| Reference | Eff. light path length (mirror displacement) | | Reflectivity (max performance) | | Detection limit (time resolution) | Accuracy | Application[a] |
|---|---|---|---|---|---|---|---|
| Ball et al. (2004) | NA[e] | | 99.9965 % | at 670 nm | 2.5 pptv ($1\sigma$, 516 s) | NA[e] | Laboratory |
| Venables et al. (2006) | 2 km (4.5 m) | at 665 nm | 99.775 % | at 665 nm | 4 pptv (NA[e], 57 s) | 14 % | Laboratory |
| Langridge et al. (2008) | 11.8 km (1.1 m) | at 660 nm | 99.9913 % | at 660 nm | 0.25 pptv ($1\sigma$, 10 s) | NA[e] | M, France |
| Varma et al. (2009)[b,c,d] | 33.5 km (8.6 m) | at 665 nm | 99.98 % | at 662 nm | 2 pptv ($1\sigma$, 5 s) | 16 % | M, Ireland |
| Kennedy et al. (2011) | 10 km (0.94 m) | | NA[e] | | 1.1 pptv ($1\sigma$, 1 s) | 11 % | M, UK |
| Wu et al. (2014) | 22 km (2 m) | | 99.991 % at [638, 672 nm] | | 7.9 pptv (NA[e], 60 s) | 12 % | Laboratory |
| Wang et al. (2017)[d] | 6.13 km (0.33 m) | at 662 nm | 99.9936 % | at 662 nm | 2.4 pptv ($1\sigma$, 1 s) | 19 % | U, China |
| Suhail et al. (2019)[b] | 6.5 km (4.5 m) | at 660 nm | 99.95 % | at 660 nm | 36 pptv (NA[e], 600 s) | NA[e] | SU, China |
| Wang and Lu (2019)[b] | 5.1 km (0.84 m) | at 665 nm | 99.985 % | at 662 nm | 3.0 pptv ($2\sigma$, 30 s) | 11 %–15 % | U, China |
| Fouqueau et al. (2020) | 3.15 km (0.82 m) | at 662 nm | 99.974 % | at 662 nm | 6 pptv (NA[e], 10 s) | 9 % | Laboratory |
| This work | 101.5 km (0.52 m) | at 662 nm | 99.9995 % | at 662 nm | 1.41 pptv ($1\sigma$, 1 s) | 10.8 % | M, Arctic |

[a] U – urban region; SU – suburban region; M – marine region. [b] Systems with open cavity. [c] Ambient $NO_3$ was well below the detection limit through the whole measurement period. [d] Average values of reflectivity are noted instead of the maximum value. [e] NA – not available.

and the physical displacement of sample in and out of ports (47.5 cm). This parameter has been commonly quantified by the injection of known amounts of standard gas such as $H_2O$ (Kennedy et al., 2011), $O_3$ (Dubé et al., 2006; Fuchs et al., 2008), and $NO_2$ (Schuster et al., 2009; Wang et al., 2017). In this study, we filled the cavity with 5 ppmv $NO_2$ standard (in $N_2$, Korea Research Institute of Standards and Science, KRISS) and compared the retrieved $NO_2$ number densities with and without the purge flow. From this experiment, we concluded that the purge volume takes 5.25 $cm^3$ in the cylindrical cell (1 in. o.d. and 1 mm thickness) and thus estimated $d_{eff}$ as 50.28 cm with an uncertainty of 5.2 % (1 % from the standard gas, 2.9 % and 2.6 % from retrieval errors, and 3.2 % from $\sigma_{NO_2}$ reported by Bogumil et al., 2003).

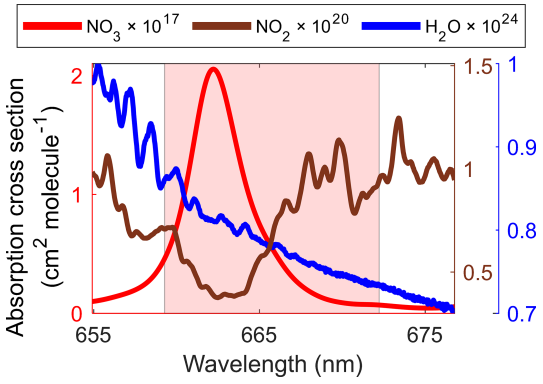


**Figure 3.** Absorption cross-sections of $NO_3$, $NO_2$, and $H_2O$ used and fitting range (shaded in light red) for number density retrievals.

### 3.2 Retrieval of number density

#### 3.2.1 Absorption cross-section, $\sigma_i$

Number density $x_i$ is determined from the optimal fit of $\sigma_i(\lambda)$ on the light extinction spectrum, $\alpha(\lambda)$, within broad spectral ranges. For $\sigma_{NO_3}$, the convolved spectrum of the literature cross-section from Yokelson et al. (1994) was used because of its simple outstanding absorption features as shown in Fig. 3. Its uncertainty was reported as 10 %.

Measured spectra were used for $H_2O$ and $NO_2$ to compensate for the imperfections in line-shape determination. These could originate from the astigmatic bias in CCD pixels and from the environmental changes (i.e., pressure and temperature) in instrumental operation conditions. In order to minimize the impacts of these accumulated errors on concentration retrievals, measured spectra were used in previous studies (Min et al., 2016; Liang et al., 2019; Barbero et al., 2020) based on the fact that the CEAS technique is widely used to characterize the wavelength-dependent light extinction properties of chemical species (Thalman and Volkamer, 2010; Axson et al., 2011; Chen and Venables, 2011; Young et al., 2011, 2014; Kahan et al., 2012; Sheps, 2013; Thalman and Volkamer, 2013; Prakash et al., 2018; Jordan et al., 2019; He et al., 2021; Wang et al., 2022).

As mentioned before, the treatment of $H_2O$ absorption features is crucial for accurate $NO_3$ measurement due to its strong but narrow absorption lines around 660 nm. To prevent this issue, the measured $H_2O$ spectrum scaled with the literature, and a relative humidity (RH) probe was used as $\sigma_{H_2O}$. For that, $H_2O$ was injected via the constant flow of ZA through a deionized water bubbler at a temperature of 22.7 °C and pressure of 991.5 hPa with 12.3 % relative humidity as averages, while an activated carbon denuder (6 mesh, Ecotech Pty Ltd., Australia) as well as a Drierite filter (8 mesh, Thermo Fisher Scientific, USA) were installed upstream of the bubbler to remove possible contaminants in the ZA cylinder. An averaged $H_2O$ spectrum from 15 min injection was scaled with the literature spectrum from the HITRAN2020 database (Gordon et al., 2022) in the range of 659.28–671.94 nm and the humidity transmitter (HMT337, Vaisala, Finland; uncertainty: 1 %) data.

Due to the weak but complex absorption features of $NO_2$ in the fitting range, we measured the absorption spectrum produced from 3 min injections of $NO_2$ standard gas (10 ppmv in $N_2$, uncertainty 1 %, KRISS) passing through a trap immersed in dry ice to ensure $H_2O$-free conditions. The acquired spectrum was scaled to the literature one from Bogumil et al. (2003) for the range of 649.64–672.79 nm, where the most apparent $NO_2$ absorption features exist with minimum fitting error.

Although the application of the measured spectra improves the fitting performance in general, the uncertainties of $\sigma_{H_2O}$ and $\sigma_{NO_2}$ inevitably increased ($\geq$ 20.1 % and 3.3 %, respectively) compared to the literature's ($\geq$ 20 % and 3.2 %), owing to the additional errors caused by the fitting procedure (1.3 % and 0.036 %) and number density calculation (0.86 % for both). Note that we only provide the lower limit error in $\sigma_{H_2O}$ propagated from the absorption line-by-line uncertainties in HITRAN2020 ($\geq$ 20 %).

#### 3.2.2 Spectral fitting

The Levenberg–Marquardt least-squares fitting software, DOASIS (Kraus, 2006), was applied for the spectral fitting of the extinction spectrum between 659.28 and 671.94 nm. A fourth-order polynomial was applied to account for the optical drift and/or unaccounted extinctions such as absorption by ambient ozone. Fit order was selected based on the resulted fitting statistics (i.e., fit coefficient uncertainties, root mean square of residuals, and chi square of residuals; Fig. S1 in the Supplement), which need to be verified for different measurement applications. The reference spectra were allowed to be shifted within $\pm$1.0 nm and squeezed freely for the $\sigma_{NO_3}$, but the measured ones were set to share the degree of horizontal shift and squeeze. Figure 4 shows an example of simultaneous retrievals of 5.45 pptv $NO_3$, 5.75 ppbv $NO_2$, and 5620 ppmv $H_2O$ with polynomial and fit residual from the ambient measurement during the Arctic shipborne mission (acquired on the open ocean on 26 August 2021, 17:11:41 UTC, described in Sect. 4) with 2 s integration time.

### 3.3 $NO_3$ wall loss evaluation

Even though CEAS is able to measure the target species without concentration calibration using chemical standards in regular operation, indeed, the loss of $NO_3$ along the airway needs to be evaluated. Many previous works carefully characterized transmission efficiency of $NO_3$ for their instruments (Aldener et al., 2006; Dubé et al., 2006; Fuchs et al., 2008; Schuster et al., 2009; Kennedy et al., 2011; Wagner et al., 2011; Hu et al., 2014; Wang et al., 2015; Sobanski et al., 2016; Wang et al., 2017; Li et al., 2018). In line with this, we conducted a series of $NO_3$ injection experiments with a custom-built $NO_3$ generation system.

#### 3.3.1 $NO_3$ generation

$NO_3$ was delivered from the synthesized $N_2O_5$ crystal under atmospheric pressure with the home-built system (Fig. 5). To produce gaseous $N_2O_5$ via Reactions (R1) and (R2), 5 % to 10 % of $O_3$ was generated by corona discharge (Nano 15, Absolute Systems Inc., Canada) of $O_2$ (300 sccm of 99.999 % $O_2$ in $N_2$, Daedeok Gas Co. Ltd.). $NO_2$ (2 % in $N_2$, AirKorea Co. Ltd.) was added in two different positions (500 and 200 sccm, respectively) into a quartz reactor (5 cm i.d. and 50 m length) for efficient production of $N_2O_5$ crystals. To minimize $HNO_3$ formation in the reactor, any $H_2O$ which can be present in the gas supplies as well as on all surfaces in the generation system was removed by heating the reactor (up to 120 °C) before the injection and by applying dry-ice traps in front of the reactor during the synthesis. After the synthesis, additional $O_3$ was introduced on white $N_2O_5$ crystals to flush out the remaining $HNO_3$ for at least 30 min. The crystals were used immediately or trapped with dry ice and stored at −78 °C for later use.

Amounts of $NO_3$ below parts per billion by volume to a few tens of parts per billion by volume were produced by thermal equilibrium, with the sublimated $N_2O_5$ introduced with a small flow of dry ZA (15–40 sccm) as a carrier gas passing the trap. Unlike previous studies (Fuchs et al., 2008; Kennedy et al., 2011; Odame-Ankrah and Osthoff, 2011; Wang et al., 2015; Wu et al., 2020), we did not provide any additional heat to shift the equilibrium towards $NO_3$ because the amount of $NO_3$ through this method was large enough to cover the ranges of typical atmospheric $NO_3$ mixing ratios in urban night conditions.

#### 3.3.2 $NO_3$ transmission efficiency, $T_{NO_3}$

$NO_3$ losses ($T_{NO_3}$) of individual parts along the airway before the detection region (i.e., overflow inlet, filter, and cavity cell) were quantified via continuous injection (at least 5 min) of the synthesized $NO_3$ under dark condition. Differences in $NO_3$ concentrations with and without each part of the flow system were acquired by periodic switching between two conditions under the same residence time using a three-way solenoid valve. In order to determine the effect of $NO_3$ loss on the aerosol-accumulated filter, filters with total ambient suspended particle loadings of 2480, 4075, and 12 308 µg were compared with a clean one.

Figure 6 presents the results of the $T_{NO_3}$ experiments for each of the test components with relative $NO_3$ concentration changes (concentrations in each step are normalized by the maximum value for every experiment resulting in ranges from 745 pptv to 169 ppbv) since a slow but steady increase in $NO_3$ concentrations was observed for all the experiments. We presumed that this drift may have been mainly due to the changes in temperature in dry-ice bath where $N_2O_5$ crystals were placed and/or the variations in contact of ZA with the crystal surface. The comparisons of the retrieved $NO_3$ with

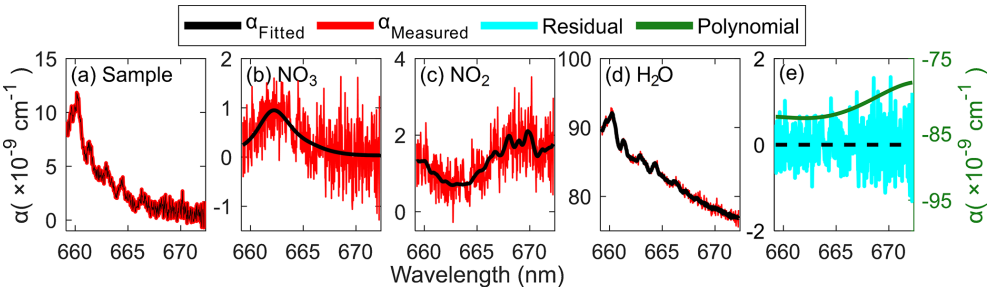


**Figure 4.** Spectral fitting example (2 s average) of ambient data; measured (red) and fitted (black) **(a)** total extinction, **(b)** $NO_3$, **(c)** $NO_2$, **(d)** $H_2O$, and **(e)** polynomial (green) with residual (cyan), respectively. Data were acquired on 26 August 2021 (UTC) from shipborne measurement on the open ocean in the Arctic region.

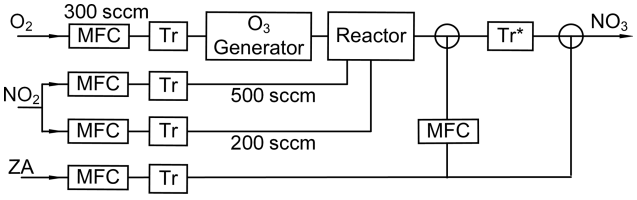


**Figure 5.** Schematic diagram of $NO_3$ generation system with flow paths (arrows). Dry-ice cold traps for $H_2O$ removal (Tr) and for sample collection (Tr*) are also shown.

and without each test part were achieved after reflecting the changes in slow increase by linear interpolations for the concentrations acquired in the same condition (shown as light red and gray dashed lines in Fig. 6).

The $T_{NO_3}$ values of individual parts are 98.9 (±1.9, 1$\sigma$), 88.1 (± 2.6), and 93.1 (± 0.3) % for coaxial overflow inlet (residence time < 0.03 s), cavity cell (residence time < 2.56 s), and filter assembly (clean case), respectively. The largest loss was observed within the cavity cell due to its relatively large surface area and long residence time compared to the other parts of the flow system. The quantified $NO_3$ loss on a clean filter surface (93.1±0.3 %) was similar to previous studies (85 (±10, 1$\sigma$) % on Aldener et al. (2006); 93 (±2) % on Dubé et al. (2006); 95 (±2) % on Fuchs et al. (2008); 84.8 (±10) % on Schuster et al. (2009); 92 (±3) % on Wang et al., 2015). Interestingly, the used filters showed no significant differences compared to the clean one regardless of the ambient aerosol loadings within the experimental range (93.1 (±0.1, 1$\sigma$), 92.9 (±0.1), and 92.7 (±2.0) % for 2480, 4075, and 12308 µg, respectively) which agree with Fuchs et al. (2008) and Zhou et al. (2018). From the results, total $T_{NO_3}$ was quantified to be 81.2 % (±2.9, 1$\sigma$) under 2.5 slpm sampling conditions.

### 3.4 Linearity tests

To test the linearity in signal response against the concentrations of species, standard injection experiments were performed. Multiple mixing ratios were achieved by regulating the degree of dilutions in synthesized $N_2O_5$ crystals, $NO_2$ standard (5 ppmv in $N_2$, KRISS; uncertainty: 1 %), and deionized water from the bubbler. As described in Sect. 3.3.2, a slow and steady increase in $NO_3$ was observed, varying from 746 to 1045 pptv under the constant dilution ratio of 1 : 150 throughout the experiment (Fig. S2). For tracking this drift in $NO_3$ standard, we alternated various dilution conditions with the base one (dilution ratio set as 1 : 150, black markers in Fig. 7a, b) and applied the linear interpolation of retrieved $NO_3$ concentrations in those conditions (gray dotted line in Fig. S2a). This baseline which depicts the changes in $NO_3$ source drift was subtracted from the data for both constant (black) and different (red) dilution conditions.

Figure 7 shows the results of standard additions with respect to the elapsed time (left) and other independent concentration evaluation parameters (right; i.e., dilution ratio for $NO_3$, nominal concentration for $NO_2$ and independent RH measurement for $H_2O$). Dashed lines in Fig. 7b, d, and f represent the correlations considering their errors (uncertainty of the parameter on $x$ axis and 1$\sigma$ variabilities in measurements on $y$ axis). The dilution ratio of $NO_3$ is calculated from the flow rate of ZA passed over the source divided by the total flow rate and $NO_2$ standard concentration is from the nominal concentration on the manufacturer's specification with the dilution ratio. RH was measured at the inlet tip by the humidity transmitter (HMT337, Vaisala, Finland) with the measurement uncertainty of 1 %.

All species show good linearities ($R^2$ of 0.9918, 0.9985, and 0.9980 for $NO_3$, $NO_2$, and $H_2O$, respectively) indicating the feasibility of atmospheric applications to those species. For $NO_2$, the intercept of 0.12 ppbv is insignificant considering the limit of detection (which will be discussed in Sect. 3.5). However, the intercept of −143 pptv in $NO_3$ is larger than the observed precision of the instrument (Sect. 3.5). This is likely due to the variabilities in our $NO_3$ source and/or the variations in offsets of slow drift correction since the source has the minimum flow rate requirements to operate. In addition, the negligible retrieved $NO_3$ (0.077 ± 1.46 pptv, average and 1$\sigma$ for 1s integration data)

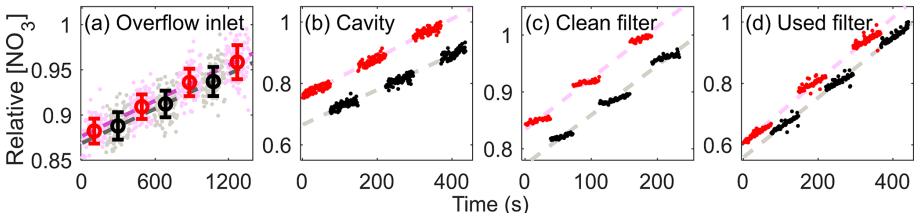


**Figure 6.** Relative $NO_3$ concentrations with (black) or without (red) test sections in **(a)** overflow inlet (averages as circle and $1\sigma$ as error bars), **(b)** cavity, and **(c)** clean and **(d)** used filter (aerosol loading of 12 308 µg). Light red and gray dashed lines represent concentration drifts inferred from linear interpolation of each condition.

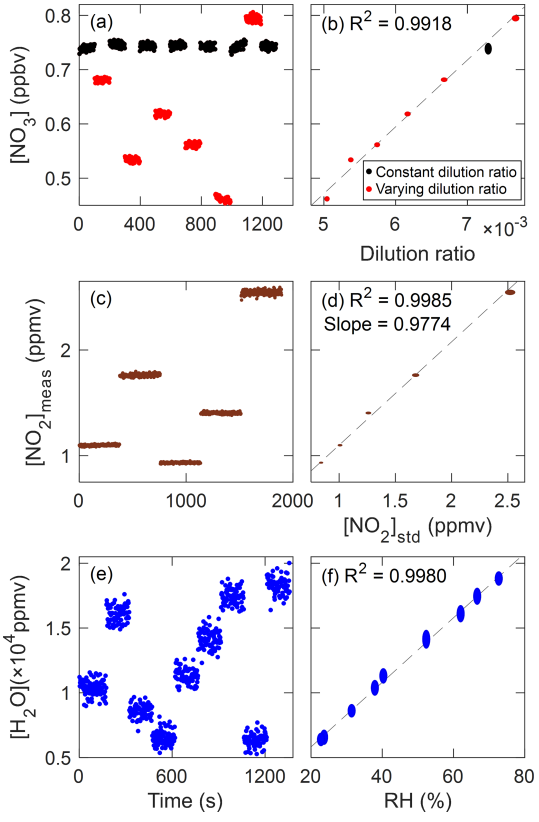


**Figure 7.** $NO_3$ **(a, b)**, $NO_2$ **(c, d)**, and $H_2O$ **(e, f)** mixing ratios with elapsed times and other independent abundance evaluation parameters in standard addition experiments. For $NO_3$, data with constant (black) and varying (red) dilution conditions were corrected for the steady drift in $NO_3$ source by linear interpolation (Fig. S2). In **(b)**, **(d)**, and **(f)** axes of the ellipses represent $1\sigma$ variability for 2 s integration data (vertical) and uncertainty of each variable (horizontal), while dashed lines show linear correlations.

during the $N_2$ injection experiment, described in Sect. 3.5, can be used as an alternative to evaluate the zero offsets.

For $H_2O$, 84 ppmv of the intercept was found, which is in a similar order of magnitude as with its precision (35 ppmv for 1 s integration time). This may be attributable to not only the random noise in detection but also the zero offset in the humidity transmitter (uncertainty: 1 %). From this highly linear response of our instrument in $H_2O$ measurements in varying atmospherically relevant ranges, we would like to emphasize that the difficulties in retrieval in $NO_3$ measurement due to $H_2O$ can be alleviated by simultaneous measurement with an instrument-specific absorption spectrum of $H_2O$ without any pre-treatment to remove it.

### 3.5 Precision and accuracy

The Allan deviation method is often used to determine the instrumental precision and the optimal integration time (Allan, 1966; Werle et al., 1993). Minimum detectable extinction for each pixel of the CCD was extracted from 1 h injection of UHP $N_2$ with 1 s integration time. Figure 8a shows the time series of the light extinction ($\alpha_{N_2}$) at 662 nm (corresponding to the 1024th pixel) where $NO_3$ absorbance peaks. $\alpha_{N_2}$ shows no significant time-dependent changes and it deviates around zero, which is likely dominated by white noise. Figure 8b shows the Allan deviation for the single pixel corresponding to 662 nm. Up to around 900 s, $1\sigma$ precision generally follows the statistical limit which implies that there are no significant integration time-dependent systematic errors up to 900 s, but it starts to gradually diverge after that, which is likely due to the instrumental drifts such as changes in conditions of the light source and/or CCD.

By only using the corresponding absorption cross-section on that single pixel, the detection limits for $NO_3$, $NO_2$, and $H_2O$ are determined to be 1.41 (0.15) pptv, 6.92 (0.73) ppbv, and 35.0 (3.69) ppmv, respectively, for 1 (60) s averaging under 1 atm and 25 °C conditions, by following Fouqueau et al. (2020). However, one should note that the spectral retrievals through the optimized fitting algorithm are likely to produce even lower detection limits than those from the single pixel because this method relies on the absorption features on broad wavelength ranges among hundreds of pixels.

Measurement uncertainties ($1\sigma$) for $NO_3$, $NO_2$, and $H_2O$ are calculated to be 10.8, 5.2, and $\geq$ 20.5 %, respectively, by Gaussian propagation of the errors in the absorption cross-section ($NO_3$: 10 %; $NO_2$: 3.3 %; and $H_2O$: $\geq$ 20.1 %), effective cavity length (3.4 %), and HR mirror reflectivity (2.2 %). Note that the fitting errors are not included here because the mathematical error varies with target species abundance. If there are strong signatures of target species in the mea-

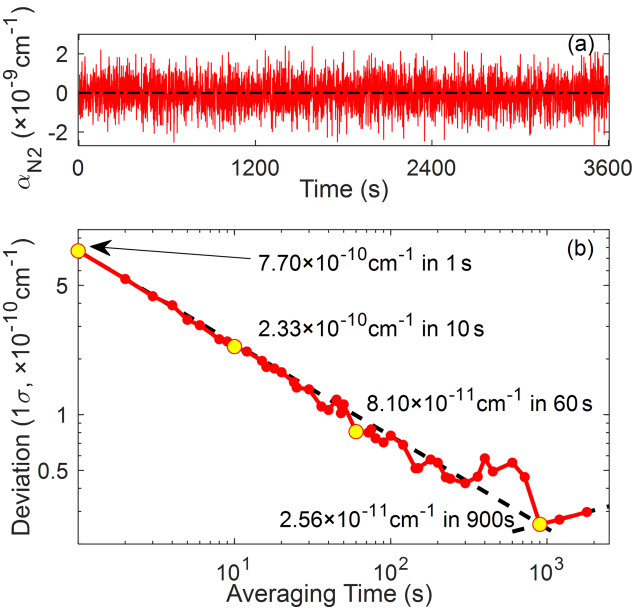


**Figure 8. (a)** Time series of light extinction for 1 h of $N_2$ injection (1 s integration) and its **(b)** Allan deviations ($1\sigma$) for the single pixel at 662 nm. Yellow circles represent deviations for 1, 10, 60, and 900 s, respectively, and the dashed line indicates the theoretical limit representing white noise (slope: $-0.5$).

surement, fitting errors are negligible. However, for the extremely low-abundance condition, the absorption features of target species weaken, and thus the fit result likely ends up producing a physically meaningless number with large error because of the limitations in numerical fitting algorithms. Hence, when the fitting error outweighs the abundance of target species, interpretations should be limited.

Table 1 summarized the cavity characteristics and performances of the existing BBCEASs for $NO_3$ measurement. Inferred detection limits with the same integration time are available in Table S1. Our instrument has the longest effective light path length even though the mirror displacement is relatively short. Since this system is able to observe the optical extinctions in the order of $10^{-10}$ cm$^{-1}$ within 1 s time resolution, we can conclude that our instrument is adequate for measuring ambient $NO_3$ abundances in terms of the sensitivity aspect. The capabilities of operation and utilization for actual application are described in the following section.

## 4 Field deployment

In order to demonstrate the feasibility of the instrument in field measurements, we deployed our system on the Korean ice breaker R/V *Araon* and operated it from late July to early September in 2021 for the expedition in the Chukchi Sea and the East Siberian Sea of the Arctic Ocean (Fig. 9a). The instrument was housed in a temperature-controlled seatainer placed on the compass deck (29 m above sea level). The inlet was installed on the window and covered by the weatherproof-designed stainless steel pipe (7.5 cm o.d.). To minimize the loss of $NO_3$ along the sampling line, air was subsampled from the center of the main flow (1 in. o.d., 1 mm thickness, PFA tubing, 20 slpm). The profile of the main flow was maintained to be steady and laminar (Reynolds number $\cong$ 1230) by the blower (DB-200, Manseung Electric Co., Korea). Total length and residence time inside the main flow was kept to be as short as possible to minimize the loss. However, due to the physical limitation of the instrument placement in the seatainer, the length of subsampled PFA tubes was elongated (length: $<$ 1 m; residence time: $<$ 1.5 s) and the total transmission efficiency of $NO_3$ for this deployment was 65.1 % ($\pm$2.14, $1\sigma$), quantified by post-campaign experiments through the same method as described in Sect. 3.3.

Aerosol filters were replaced by an integrated auto-filter changer (Dubé et al., 2006) only during the early and later stage of the mission near the coastal region of northeast Asia for every 3 h and manually changed with intervals of 4 to 6 h in remote regions since the demands for changing the filter were scarce due to the low aerosol loading in the Arctic region. The $R(\lambda)$ and $I_{\mathrm{out},0}(\lambda)$ were checked every 2 h and instantaneously interpolated for real-time $\alpha(\lambda)$ calculation. During the campaign, $R(\lambda = 662\,\mathrm{nm})$ were varying in the range from 99.9985 % to 99.9989 %, which are lower than the best performances of the instrument in the laboratory, mainly due to the difference in proficiency and environment for cleaning optics, but still high enough for ambient monitoring of $NO_3$. The negligible change in $R$ is direct evidence that our vibration-resistant design is robust despite the strong vibrations in the platform due to the sea ice breaking activities. During the mission, the averages ($\pm 1\sigma$) of temperature and pressure of the sample in the cavity were 22.02 ($\pm$0.90) °C and 997.6($\pm$25.9) hPa. And the changes in absorption cross-sections due to these variations were too small to be detected by our instrument.

Figure 9b–d show the time series of $H_2O$, $NO_2$, and $NO_3$ (1 min averaged), as well as $O_3$ monitored by the UV absorption instrument (49i, Thermo Fisher Scientific, USA), radiance (CNR4, Kipp & Zonen, Netherland) and production rate of $NO_3$, $P(NO_3)$, calculated as Eq. (3). For $H_2O$, our measurements were compared to the calculated values from the pressure (PTB110, Vaisala, Finland), relative humidity, and temperature (HMP155, Vaisala, Finland) data measured on the mainmast of the icebreaker. Here we only show the selected period (23 August 2021 at 17:00 UTC to 25 August 2021 at 15:10 UTC) when the $NO_3$ signals were continuously observed well above the detection limit. $H_2O$ mixing ratios measured by our instrument ranged from 4160 to 6510 ppmv (mean of 5580 ppmv) and average (maximum) value(s) of $NO_2$ and $NO_3$ were 3.21 (23.9) ppbv and 2.53 (9.51) pptv, respectively. $H_2O$ concentrations measured by both instruments were in good agreement considering the uncertainty

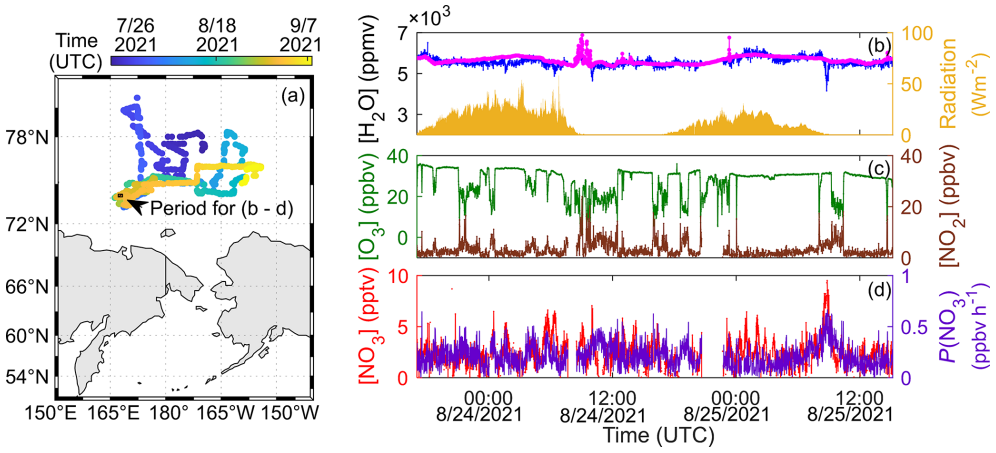


**Figure 9. (a)** A map with cruise track of R/V *Araon* and **(b–d)** representative time series of 1 min averaged $H_2O$ (measured by our instrument on compass deck in blue and a Vaisala instrument on the mainmast in pink), radiation, $O_3$, $NO_2$, and $NO_3$ with a calculated production rate of $NO_3$ for 23 August 2021 at 17:00 UTC to 25 August 2021 at 15:10 UTC on the open ocean in the Arctic region.

of $H_2O$ for our instrument ($\geq 20.5\,\%$).

$$P(NO_3) = k_{R1}[NO_2][O_3] \quad (3)$$

During the campaign, several fresh emissions from R/V *Araon* were observed, represented by sharp changes in $O_3$ and $NO_2$ as shown in Fig. 9c indicating that $O_3$ was titrated by NO and formed $NO_2$. These exhaust emissions lasted from a few minutes to several hours depending on the atmospheric conditions such as wind direction and atmospheric stability as well as movement of the vessel (i.e., sailing or anchoring in one place for marine survey).

$P(NO_3)$ was generally small but rose up to 0.66 ppbv $h^{-1}$ (mean of 0.21 ppbv $h^{-1}$) depending on whether the sampled air masses were directly influenced by the ship plumes or not but were still lower than those observed in previous works during summertime: 0.31 ppbv $h^{-1}$ in rural areas (Geyer et al., 2001a) and 1.10–3.2 ppbv $h^{-1}$ in urban areas (Wang et al., 2013; Brown et al., 2017; Zhou et al., 2018). Within the plume condition, maximum $NO_3$ increased up to 1.85 pptv even though there was sunlight at that time. The trend of $NO_3$ concentration was well-matched with $P(NO_3)$ for most of the period indicating the suitability of our instrument for ambient $NO_3$ measurements. Further analysis related to regional impacts of ship plume chemistry together with $NO_3$ oxidation assessment with observed VOCs and DMS would be interesting topics for future studies.

## 5 Conclusions

This paper describes our newly built cavity-enhanced absorption spectrometer for simultaneous measurements of ambient $NO_3$, $NO_2$, and $H_2O$ from their absorption features in 659.28–671.94 nm. High performances in measurement capabilities and simplicity in maintaining and processing schemes were achieved by applying high-reflection mirrors (up to 99.9995 % at 662 nm), by integrating the mirror purge and cage system as well as by simultaneous quantification of $H_2O$ using its measured spectrum. Generally, the light at 662 nm travels more than 40 km (up to 101.5 km) within the compact cavity cell (51.5 cm), which enables sensitive measurements of the target species. To overcome the difficulties in $H_2O$ treatment for accurate $NO_3$ measurement, the measured absorption spectrum of $H_2O$ was used and our instrument showed high linearity for varying atmospherically relevant ranges of $H_2O$. The transmission efficiency of $NO_3$ from the inlet tip to the detection region was evaluated as 81.2 ($\pm$2.9, 1$\sigma$) % within the residence time of 2.59 s from the prepared $NO_3$ addition experiments. Consequently, for $NO_3$, $NO_2$, and $H_2O$, the measurement accuracies and detection limit (1$\sigma$, 1 s, estimated from a single-pixel CCD) were determined as 10.8 %, 4.7 %, and $\geq$ 20.5 % with 1.41 pptv, 6.92 ppbv, and 35.0 ppmv, respectively, which are sufficiently low for ambient applications.

The instrument was successfully deployed aboard the Korean ice breaker R/V *Araon* and captured not only the background condition of the atmosphere over the open ocean in the Arctic but also the highly structured features of the plumes which originated from the vessel exhaust during the campaign. In addition, the trend of $NO_3$ concentration was well-matched with the calculated $P(NO_3)$, which serves as a proof of the potential for active applications of this instrument in further studies not only in urban regions but also in pristine regions with any mobile platforms including aircraft and research vessels.

*Data availability.* The datasets used in this study are available upon request to the corresponding author, Kyung-Eun Min (kemin@gist.ac.kr).

*Supplement.* The supplement related to this article is available online at: https://doi.org/10.5194/amt-15-4473-2022-supplement.

*Author contributions.* WN and KEM contributed to designing and performing this study. TSR provided the data for $O_3$ and helped with the field deployment. WN and KEM wrote the paper with contributions from CC and BP. All co-authors revised the content of the original paper and approved the final version of the paper.

*Competing interests.* The contact author has declared that none of the authors has any competing interests.

*Disclaimer.* Publisher's note: Copernicus Publications remains neutral with regard to jurisdictional claims in published maps and institutional affiliations.

*Acknowledgements.* We thank all the crew members of R/V *Araon* for their support on the mission.

*Financial support.* This research has been supported by the Korea Polar Research Institute (grant no. PE21900) and the Korea Environmental Industry and Technology Institute (grant no. 2019000160004).

*Review statement.* This paper was edited by Marc von Hobe and reviewed by two anonymous referees.

## References

Aldener, M., Brown, S. S., Stark, H., Williams, E. J., Lerner, B. M., Kuster, W. C., Goldan, P. D., Quinn, P. K., Bates, T. S., Fehsenfeld, F. C., and Ravishankara, A. R.: Reactivity and loss mechanisms of $NO_3$ and $N_2O_5$ in a polluted marine environment: Results from in situ measurements during New England Air Quality Study 2002, J. Geophys. Res.-Atmos., 111, D23S73, https://doi.org/10.1029/2006jd007252, 2006.

Allan, B. J., Carslaw, N., Coe, H., Burgess, R. A., and Plane, J. M. C.: Observations of the nitrate radical in the marine boundary layer, J. Atmos. Chem., 33, 129–154, https://doi.org/10.1023/a:1005917203307, 1999.

Allan, B. J., McFiggans, G., Plane, J. M. C., Coe, H., and McFadyen, G. G.: The nitrate radical in the remote marine boundary layer, J. Geophys. Res.-Atmos., 105, 24191–24204, https://doi.org/10.1029/2000jd900314, 2000.

Allan, D. W.: Statistics of atomic frequency standards, Proc. IEEE, 54, 221–230, https://doi.org/10.1109/proc.1966.4634, 1966.

Asaf, D., Pedersen, D., Matveev, V., Peleg, M., Kern, C., Zingler, J., Platt, U., and Luria, M.: Long-term measurements of $NO_3$ radical at a semiarid urban site: 1. Extreme concentration events and their oxidation capacity, Environ. Sci. Technol., 43, 9117–9123, https://doi.org/10.1021/es900798b, 2009.

Axson, J. L., Washenfelder, R. A., Kahan, T. F., Young, C. J., Vaida, V., and Brown, S. S.: Absolute ozone absorption cross section in the Huggins Chappuis minimum (350–470 nm) at 296 K, Atmos. Chem. Phys., 11, 11581–11590, https://doi.org/10.5194/acp-11-11581-2011, 2011.

Ayers, J. D., Apodaca, R. L., Simpson, W. R., and Baer, D. S.: Off-axis cavity ringdown spectroscopy: application to atmospheric nitrate radical detection, Appl. Opt., 44, 7239–7242, https://doi.org/10.1364/AO.44.007239, 2005.

Ball, S. M. and Jones, R. L.: Broad-band cavity ringdown spectroscopy, Chem. Rev., 103, 5239–5262, https://doi.org/10.1021/cr020523k, 2003.

Ball, S. M., Langridge, J. M., and Jones, R. L.: Broadband cavity enhanced absorption spectroscopy using light emitting diodes, Chem. Phys. Lett., 398, 68–74, https://doi.org/10.1016/j.cplett.2004.08.144, 2004.

Barbero, A., Blouzon, C., Savarino, J., Caillon, N., Dommergue, A., and Grilli, R.: A compact incoherent broadband cavity-enhanced absorption spectrometer for trace detection of nitrogen oxides, iodine oxide and glyoxal at levels below parts per billion for field applications, Atmos. Meas. Tech., 13, 4317–4331, https://doi.org/10.5194/amt-13-4317-2020, 2020.

Bodhaine, B. A., Wood, N. B., Dutton, E. G., and Slusser, J. R.: On Rayleigh optical depth calculations, J. Atmos. Ocean. Technol., 16, 1854–1861, https://doi.org/10.1175/1520-0426(1999)016<1854:orodc>2.0.co;2, 1999.

Bogumil, K., Orphal, J., Homann, T., Voigt, S., Spietz, P., Fleischmann, O. C., Vogel, A., Hartmann, M., Kromminga, H., Bovensmann, H., Frerick, J., and Burrows, J. P.: Measurements of molecular absorption spectra with the SCIAMACHY pre-flight model: instrument characterization and reference data for atmospheric remote-sensing in the 230–2380 nm region, J. Photochem. Photobiol. A, 157, 167–184, https://doi.org/10.1016/s1010-6030(03)00062-5, 2003.

Brown, S. S. and Stutz, J.: Nighttime radical observations and chemistry, Chem. Soc. Rev., 41, 6405, https://doi.org/10.1039/c2cs35181a, 2012.

Brown, S. S., Stark, H., Ciciora, S. J., and Ravishankara, A. R.: In-situ measurement of atmospheric $NO_3$ and $N_2O_5$ via cavity ring-down spectroscopy, Geophys. Res. Lett., 28, 3227–3230, https://doi.org/10.1029/2001gl013303, 2001.

Brown, S. S., Osthoff, H. D., Stark, H., Dubé, W. P., Ryerson, T. B., Warneke, C., De Gouw, J. A., Wollny, A. G., Parrish, D. D., Fehsenfeld, F. C., and Ravishankara, A. R.: Aircraft observations of daytime $NO_3$ and $N_2O_5$ and their implications for tropospheric chemistry, J. Photochem. Photobiol., A, 176, 270–278, https://doi.org/10.1016/j.jphotochem.2005.10.004, 2005.

Brown, S. S., Dubé, W. P., Tham, Y. J., Zha, Q., Xue, L., Poon, S., Wang, Z., Blake, D. R., Tsui, W., Parrish, D. D., and Wang, T.: Nighttime chemistry at a high altitude site above Hong Kong, J. Geophys. Res.-Atmos., 121, 2457–2475, https://doi.org/10.1002/2015jd024566, 2016.

Brown, S. S., An, H., Lee, M., Park, J.-H., Lee, S.-D., Fibiger, D. L., McDuffie, E. E., Dubé, W. P., Wagner, N. L., and Min, K.-E.: Cavity enhanced spectroscopy for measurement of nitrogen oxides in the Anthropocene: results from the Seoul tower during MAPS 2015, Faraday Discuss., 200, 529–557, https://doi.org/10.1039/c7fd00001d, 2017.

Chang, Y., Zhang, Y., Tian, C., Zhang, S., Ma, X., Cao, F., Liu, X., Zhang, W., Kuhn, T., and Lehmann, M. F.: Nitrogen isotope fractionation during gas-to-particle conversion of $NO_x$ to $NO_3^-$ in the atmosphere – implications for isotope-based $NO_x$ source apportionment, Atmos. Chem. Phys., 18, 11647–11661, https://doi.org/10.5194/acp-18-11647-2018, 2018.

Chen, J. and Venables, D. S.: A broadband optical cavity spectrometer for measuring weak near-ultraviolet absorption spectra of gases, Atmos. Meas. Tech., 4, 425–436, https://doi.org/10.5194/amt-4-425-2011, 2011.

Dorn, H.-P., Apodaca, R. L., Ball, S. M., Brauers, T., Brown, S. S., Crowley, J. N., Dubé, W. P., Fuchs, H., Häseler, R., Heitmann, U., Jones, R. L., Kiendler-Scharr, A., Labazan, I., Langridge, J. M., Meinen, J., Mentel, T. F., Platt, U., Pöhler, D., Rohrer, F., Ruth, A. A., Schlosser, E., Schuster, G., Shillings, A. J. L., Simpson, W. R., Thieser, J., Tillmann, R., Varma, R., Venables, D. S., and Wahner, A.: Intercomparison of $NO_3$ radical detection instruments in the atmosphere simulation chamber SAPHIR, Atmos. Meas. Tech., 6, 1111–1140, https://doi.org/10.5194/amt-6-1111-2013, 2013.

Dubé, W. P., Brown, S. S., Osthoff, H. D., Nunley, M. R., Ciciora, S. J., Paris, M. W., McLaughlin, R. J., and Ravishankara, A. R.: Aircraft instrument for simultaneous, in situ measurement of $NO_3$ and $N_2O_5$ via pulsed cavity ring-down spectroscopy, Rev. Sci. Instrum., 77, 034101, https://doi.org/10.1063/1.2176058, 2006.

Fiedler, S. E., Hese, A., and Ruth, A. A.: Incoherent broad-band cavity-enhanced absorption spectroscopy, Chem. Phys. Lett., 371, 284–294, https://doi.org/10.1016/s0009-2614(03)00263-x, 2003.

Flemmer, M. M. and Ham, J. E.: Cavity ring-down spectroscopy with an automated control feedback system for investigating nitrate radical surface chemistry reactions, Rev. Sci. Instrum., 83, 085103, https://doi.org/10.1063/1.4739768, 2012.

Foulds, A., Khan, M. A. H., Bannan, T. J., Percival, C. J., Lowenberg, M. H., and Shallcross, D. E.: Abundance of $NO_3$ derived organo-nitrates and their importance in the atmosphere, Atmosphere, 12, 1381, https://doi.org/10.3390/atmos12111381, 2021.

Fouqueau, A., Cirtog, M., Cazaunau, M., Pangui, E., Zapf, P., Siour, G., Landsheere, X., Méjean, G., Romanini, D., and Picquet-Varrault, B.: Implementation of an incoherent broadband cavity-enhanced absorption spectroscopy technique in an atmospheric simulation chamber for in situ $NO_3$ monitoring: characterization and validation for kinetic studies, Atmos. Meas. Tech., 13, 6311–6323, https://doi.org/10.5194/amt-13-6311-2020, 2020.

Fuchs, H., Dubeì, W. P., Ciciora, S. J., and Brown, S. S.: Determination of inlet transmission and conversion efficiencies for in situ measurements of the nocturnal nitrogen oxides, $NO_3$, $N_2O_5$ and $NO_2$, via pulsed cavity ring-down spectroscopy, Anal. Chem., 80, 6010–6017, https://doi.org/10.1021/ac8007253, 2008.

Gagliardi, G. and Loock, H. P. (Eds.): Cavity-enhanced spectroscopy and sensing, 179, Springer, Berlin, Heidelberg, https://doi.org/10.1007/978-3-642-40003-2, 2014.

Geyer, A., Ackermann, R., Dubois, R., Lohrmann, B., Müller, T., and Platt, U.: Long-term observation of nitrate radicals in the continental boundary layer near Berlin, Atmos. Environ., 35, 3619–3631, https://doi.org/10.1016/s1352-2310(00)00549-5, 2001a.

Geyer, A., Alicke, B., Konrad, S., Schmitz, T., Stutz, J., and Platt, U.: Chemistry and oxidation capacity of the nitrate radical in the continental boundary layer near Berlin, J. Geophys. Res.-Atmos., 106, 8013–8025, https://doi.org/10.1029/2000jd900681, 2001b.

Geyer, A., Alicke, B., Ackermann, R., Martinez, M., Harder, H., Brune, W., di Carlo, P., Williams, E., Jobson, T., and Hall, S.: Direct observations of daytime $NO_3$: Implications for urban boundary layer chemistry, J. Geophys. Res.-Atmos., 108, https://doi.org/10.1029/2002jd002967, 2003.

Gordon, I. E., Rothman, L. S., Hargreaves, R. J., Hashemi, R., Karlovets, E. V., Skinner, F. M., Conway, E. K., Hill, C., Kochanov, R. V., Tan, Y., Wcisło, P., Finenko, A. A., Nelson, K., Bernath, P. F., Birk, M., Boudon, V., Campargue, A., Chance, K. V., Coustenis, A., Drouin, B. J., Flaud, J. M., Gamache, R. R., Hodges, J. T., Jacquemart, D., Mlawer, E. J., Nikitin, A. V., Perevalov, V. I., Rotger, M., Tennyson, J., Toon, G. C., Tran, H., Tyuterev, V. G., Adkins, E. M., Baker, A., Barbe, A., Canè, E., Császár, A. G., Dudaryonok, A., Egorov, O., Fleisher, A. J., Fleurbaey, H., Foltynowicz, A., Furtenbacher, T., Harrison, J. J., Hartmann, J. M., Horneman, V. M., Huang, X., Karman, T., Karns, J., Kassi, S., Kleiner, I., Kofman, V., Kwabia–Tchana, F., Lavrentieva, N. N., Lee, T. J., Long, D. A., Lukashevskaya, A. A., Lyulin, O. M., Makhnev, V. Y., Matt, W., Massie, S. T., Melosso, M., Mikhailenko, S. N., Mondelain, D., Müller, H. S. P., Naumenko, O. V., Perrin, A., Polyansky, O. L., Raddaoui, E., Raston, P. L., Reed, Z. D., Rey, M., Richard, C., Tóbiás, R., Sadiek, I., Schwenke, D. W., Starikova, E., Sung, K., Tamassia, F., Tashkun, S. A., Vander Auwera, J., Vasilenko, I. A., Vigasin, A. A., Villanueva, G. L., Vispoel, B., Wagner, G., Yachmenev, A., and Yurchenko, S. N.: The HITRAN2020 molecular spectroscopic database, J. Quant. Spectrosc. Ra. Trans., 277, 107949, https://doi.org/10.1016/j.jqsrt.2021.107949, 2022.

He, Q., Fang, Z., Shoshanim, O., Brown, S. S., and Rudich, Y.: Scattering and absorption cross sections of atmospheric gases in the ultraviolet–visible wavelength range (307–725 nm), Atmos. Chem. Phys., 21, 14927–14940, https://doi.org/10.5194/acp-21-14927-2021, 2021.

Heintz, F., Platt, U., Flentje, H., and Dubois, R.: Long-term observation of nitrate radicals at the Tor Station, Kap Arkona (Rügen), J. Geophys. Res.-Atmos., 101, 22891–22910, https://doi.org/10.1029/96jd01549, 1996.

Hu, R.-Z., Wang, D., Xie, P.-H., Ling, L.-Y., Qin, M., Li, C.-X., and Liu, J.-G.: Diode laser cavity ring-down spectroscopy for atmospheric $NO_3$ radical measurement, Acta. Phys. Sin., 63, 110707, https://doi.org/10.7498/aps.63.110707, 2014.

Jordan, N., Ye, C. Z., Ghosh, S., Washenfelder, R. A., Brown, S. S., and Osthoff, H. D.: A broadband cavity-enhanced spectrometer for atmospheric trace gas measurements and Rayleigh scattering cross sections in the cyan region (470–540 nm), Atmos. Meas. Tech., 12, 1277–1293, https://doi.org/10.5194/amt-12-1277-2019, 2019.

Kahan, T. F., Washenfelder, R. A., Vaida, V., and Brown, S. S.: Cavity-enhanced measurements of hydrogen peroxide absorption cross sections from 353 to 410 nm, J. Phys. Chem., 116, 5941–5947, https://doi.org/10.1021/jp2104616, 2012.

Kennedy, O. J., Ouyang, B., Langridge, J. M., Daniels, M. J. S., Bauguitte, S., Freshwater, R., McLeod, M. W., Ironmonger, C., Sendall, J., Norris, O., Nightingale, R., Ball, S. M., and Jones, R. L.: An aircraft based three channel broadband cavity enhanced absorption spectrometer for simultaneous measurements

of $NO_3$, $N_2O_5$ and $NO_2$, Atmos. Meas. Tech., 4, 1759–1776, https://doi.org/10.5194/amt-4-1759-2011, 2011.

King, M., Dick, E., and Simpson, W.: A new method for the atmospheric detection of the nitrate radical ($NO_3$), Atmos. Environ., 34, 685–688, https://doi.org/10.1016/S1352-2310(99)00418-5, 2000.

Kraus, S.: DOASIS a framework design for DOAS, PhD thesis, University of Heidelberg, Heidelberg, Germany, https://hci.iwr.uni-heidelberg.de/content/doasis-framework-design-doas (last access: 7 March 2022), 2006.

Langridge, J. M., Ball, S. M., Shillings, A. J. L., and Jones, R. L.: A broadband absorption spectrometer using light emitting diodes for ultrasensitive, in situ trace gas detection, Rev. Sci. Instrum., 79, 123110, https://doi.org/10.1063/1.3046282, 2008.

Le Breton, M., Hallquist, Å. M., Pathak, R. K., Simpson, D., Wang, Y., Johansson, J., Zheng, J., Yang, Y., Shang, D., Wang, H., Liu, Q., Chan, C., Wang, T., Bannan, T. J., Priestley, M., Percival, C. J., Shallcross, D. E., Lu, K., Guo, S., Hu, M., and Hallquist, M.: Chlorine oxidation of VOCs at a semi-rural site in Beijing: significant chlorine liberation from $ClNO_2$ and subsequent gas- and particle-phase Cl–VOC production, Atmos. Chem. Phys., 18, 13013–13030, https://doi.org/10.5194/acp-18-13013-2018, 2018.

Li, S., Liu, W., Xie, P., Li, A., Qin, M., and Dou, K.: Measurements of nighttime nitrate radical concentrations in the atmosphere by long-path differential optical absorption spectroscopy, Adv. Atmos. Sci., 24, 875–880, https://doi.org/10.1007/s00376-007-0875-2, 2007.

Li, Z., Hu, R., Xie, P., Chen, H., Wu, S., Wang, F., Wang, Y., Ling, L., Liu, J., and Liu, W.: Development of a portable cavity ring down spectroscopy instrument for simultaneous, in situ measurement of $NO_3$ and $N_2O_5$, Opt. Express, 26, A433–A449, https://doi.org/10.1364/OE.26.00A433, 2018.

Liang, S., Qin, M., Xie, P., Duan, J., Fang, W., He, Y., Xu, J., Liu, J., Li, X., Tang, K., Meng, F., Ye, K., Liu, J., and Liu, W.: Development of an incoherent broadband cavity-enhanced absorption spectrometer for measurements of ambient glyoxal and NO2 in a polluted urban environment, Atmos. Meas. Tech., 12, 2499–2512, https://doi.org/10.5194/amt-12-2499-2019, 2019.

Lin, Y.-C., Zhang, Y.-L., Fan, M.-Y., and Bao, M.: Heterogeneous formation of particulate nitrate under ammonium-rich regimes during the high-PM2.5 events in Nanjing, China, Atmos. Chem. Phys., 20, 3999–4011, https://doi.org/10.5194/acp-20-3999-2020, 2020.

Liu, L., Bei, N., Hu, B., Wu, J., Liu, S., Li, X., Wang, R., Liu, Z., Shen, Z., and Li, G.: Wintertime nitrate formation pathways in the north China plain: Importance of $N_2O_5$ heterogeneous hydrolysis, Environ. Pollut., 266, 115287, https://doi.org/10.1016/j.envpol.2020.115287, 2020.

Lu, X., Qin, M., Xie, P.-H., Duan, J., Fang, W., Ling, L.-Y., Shen, L.-L., Liu, J.-G., and Liu, W.-Q.: Measurements of atmospheric $NO_3$ radicals in Hefei using LED-based long path differential optical absorption spectroscopy, Chin. Phys. B, 25, 024210, https://doi.org/10.1088/1674-1056/25/2/024210, 2016.

Matsumoto, J., Kosugi, N., Imai, H., and Kajii, Y.: Development of a measurement system for nitrate radical and dinitrogen pentoxide using a thermal conversion/laser-induced fluorescence technique, Rev. Sci. Instrum., 76, 064101, https://doi.org/10.1063/1.1927098, 2005.

McDuffie, E. E., Womack, C. C., Fibiger, D. L., Dube, W. P., Franchin, A., Middlebrook, A. M., Goldberger, L., Lee, B. H., Thornton, J. A., Moravek, A., Murphy, J. G., Baasandorj, M., and Brown, S. S.: On the contribution of nocturnal heterogeneous reactive nitrogen chemistry to particulate matter formation during wintertime pollution events in Northern Utah, Atmos. Chem. Phys., 19, 9287–9308, https://doi.org/10.5194/acp-19-9287-2019, 2019.

McLaren, R., Salmon, R. A., Liggio, J., Hayden, K. L., Anlauf, K. G., and Leaitch, W. R.: Nighttime chemistry at a rural site in the Lower Fraser Valley, Atmos. Environ., 38, 5837–5848, https://doi.org/10.1016/j.atmosenv.2004.03.074, 2004.

Mihelcic, D., Klemp, D., Müsgen, P., Pätz, H. W., and Volz-Thomas, A.: Simultaneous measurements of peroxy and nitrate radicals at Schauinsland, J. Atmos. Chem., 16, 313–335, https://doi.org/10.1007/bf01032628, 1993.

Min, K.-E., Washenfelder, R. A., Dubé, W. P., Langford, A. O., Edwards, P. M., Zarzana, K. J., Stutz, J., Lu, K., Rohrer, F., Zhang, Y., and Brown, S. S.: A broadband cavity enhanced absorption spectrometer for aircraft measurements of glyoxal, methylglyoxal, nitrous acid, nitrogen dioxide, and water vapor, Atmos. Meas. Tech., 9, 423–440, https://doi.org/10.5194/amt-9-423-2016, 2016.

Nakayama, T., Ide, T., Taketani, F., Kawai, M., Takahashi, K., and Matsumi, Y.: Nighttime measurements of ambient $N_2O_5$, $NO_2$, NO and $O_3$ in a sub-urban area, Toyokawa, Japan, Atmos. Environ., 42, 1995–2006, https://doi.org/10.1016/j.atmosenv.2007.12.001, 2008.

Ng, N. L., Brown, S. S., Archibald, A. T., Atlas, E., Cohen, R. C., Crowley, J. N., Day, D. A., Donahue, N. M., Fry, J. L., Fuchs, H., Griffin, R. J., Guzman, M. I., Herrmann, H., Hodzic, A., Iinuma, Y., Jimenez, J. L., Kiendler-Scharr, A., Lee, B. H., Luecken, D. J., Mao, J., McLaren, R., Mutzel, A., Osthoff, H. D., Ouyang, B., Picquet-Varrault, B., Platt, U., Pye, H. O. T., Rudich, Y., Schwantes, R. H., Shiraiwa, M., Stutz, J., Thornton, J. A., Tilgner, A., Williams, B. J., and Zaveri, R. A.: Nitrate radicals and biogenic volatile organic compounds: oxidation, mechanisms, and organic aerosol, Atmos. Chem. Phys., 17, 2103–2162, https://doi.org/10.5194/acp-17-2103-2017, 2017.

Noxon, J. F., Norton, R. B., and Marovich, E.: $NO_3$ in the troposphere, Geophys. Res. Lett., 7, 125–128, https://doi.org/10.1029/GL007i002p00125, 1980.

Odame-Ankrah, C. A. and Osthoff, H. D.: A compact diode laser cavity ring-down spectrometer for atmospheric measurements of $NO_3$ and $N_2O_5$ with automated zeroing and calibration, Appl. Spectrosc., 65, 1260–1268, https://doi.org/10.1366/11-06384, 2011.

Osthoff, H. D., Sommariva, R., Baynard, T., Pettersson, A., Williams, E. J., Lerner, B. M., Roberts, J. M., Stark, H., Goldan, P. D., Kuster, W. C., Bates, T. S., Coffman, D., Ravishankara, A. R., and Brown, S. S.: Observation of daytime $N_2O_5$ in the marine boundary layer during New England Air Quality Study-Intercontinental Transport and Chemical Transformation 2004, J. Geophys. Res.-Atmos., 111, D23S14, https://doi.org/10.1029/2006jd007593, 2006.

Osthoff, H. D., Roberts, J. M., Ravishankara, A. R., Williams, E. J., Lerner, B. M., Sommariva, R., Bates, T. S., Coffman, D., Quinn, P. K., Dibb, J. E., Stark, H., Burkholder, J. B., Talukdar, R. K., Meagher, J., Fehsenfeld, F. C., and Brown, S. S.: High levels

of nitryl chloride in the polluted subtropical marine boundary layer, Nat. Geosci., 1, 324–328, https://doi.org/10.1038/ngeo177, 2008.

Platt, U., Perner, D., Winer, A. M., Harris, G. W., and Pitts, J. N. J.: Detection of $NO_3$ in the polluted troposphere by differential optical absorption, Geophys. Res. Lett., 7, 89–92, 1980.

Prakash, N., Ramachandran, A., Varma, R., Chen, J., Mazzoleni, C., and Du, K.: Near-infrared incoherent broadband cavity enhanced absorption spectroscopy (NIR-IBBCEAS) for detection and quantification of natural gas components, Analyst., 143, 3284–3291, https://doi.org/10.1039/c8an00819a, 2018.

Roberts, J. M., Osthoff, H. D., Brown, S. S., and Ravishankara, A. R.: $N_2O_5$ oxidizes chloride to $Cl_2$ in acidic atmospheric aerosol, Science, 321, 1059–1059, https://doi.org/10.1126/science.1158777, 2008.

Schuster, G., Labazan, I., and Crowley, J. N.: A cavity ring down/cavity enhanced absorption device for measurement of ambient $NO_3$ and $N_2O_5$, Atmos. Meas. Tech., 2, 1–13, https://doi.org/10.5194/amt-2-1-2009, 2009.

Shardanand, S. and Rao, A. P.: Absolute Rayleigh scattering cross sections of gases and freons of stratospheric interest in the visible and ultraviolet regions, NASA Technical Note, TN-D-8442, 1977.

Sheps, L.: Absolute ultraviolet absorption spectrum of a Criegee intermediate $CH_2OO$, J. Phys. Chem. Lett., 4, 4201–4205, https://doi.org/10.1021/jz402191w, 2013.

Simpson, W. R.: Continuous wave cavity ring-down spectroscopy applied toin situdetection of dinitrogen pentoxide ($N_2O_5$), Rev. Sci. Instrum., 74, 3442–3452, https://doi.org/10.1063/1.1578705, 2003.

Sobanski, N., Schuladen, J., Schuster, G., Lelieveld, J., and Crowley, J. N.: A five-channel cavity ring-down spectrometer for the detection of $NO_2$, $NO_3$, $N_2O_5$, total peroxy nitrates and total alkyl nitrates, Atmos. Meas. Tech., 9, 5103–5118, https://doi.org/10.5194/amt-9-5103-2016, 2016.

Sommariva, R., Pilling, M. J., Bloss, W. J., Heard, D. E., Lee, J. D., Fleming, Z. L., Monks, P. S., Plane, J. M. C., Saiz-Lopez, A., Ball, S. M., Bitter, M., Jones, R. L., Brough, N., Penkett, S. A., Hopkins, J. R., Lewis, A. C., and Read, K. A.: Nighttime radical chemistry during the NAMBLEX campaign, Atmos. Chem. Phys., 7, 587–598, https://doi.org/10.5194/acp-7-587-2007, 2007.

Stark, H., Lerner, B. M., Schmitt, R., Jakoubek, R., Williams, E. J., Ryerson, T. B., Sueper, D. T., Parrish, D. D., and Fehsenfeld, F. C.: Atmospheric in situ measurement of nitrate radical ($NO_3$) and other photolysis rates using spectroradiometry and filter radiometry, J. Geophys. Res.-Atmos., 112, D10S04, https://doi.org/10.1029/2006jd007578, 2007.

Stutz, J., Alicke, B., Ackermann, R., Geyer, A., White, A., and Williams, E.: Vertical profiles of $NO_3$, $N_2O_5$, $O_3$, and $NO_x$ in the nocturnal boundary layer: 1. Observations during the Texas Air Quality Study 2000, J. Geophys. Res.-Atmos., 109, https://doi.org/10.1029/2003jd004209, 2004.

Suhail, K., George, M., Chandran, S., Varma, R., Venables, D. S., Wang, M., and Chen, J.: Open path incoherent broadband cavity-enhanced measurements of $NO_3$ radical and aerosol extinction in the North China Plain, Spectrochim. Acta A Mol. Biomol. Spectrosc., 208, 24–31, https://doi.org/10.1016/j.saa.2018.09.023, 2019.

Thalman, R. and Volkamer, R.: Inherent calibration of a blue LED-CE-DOAS instrument to measure iodine oxide, glyoxal, methyl glyoxal, nitrogen dioxide, water vapour and aerosol extinction in open cavity mode, Atmos. Meas. Tech., 3, 1797–1814, https://doi.org/10.5194/amt-3-1797-2010, 2010.

Thalman, R. and Volkamer, R.: Temperature dependent absorption cross-sections of $O_2$–$O_2$ collision pairs between 340 and 630 nm and at atmospherically relevant pressure, Phys. Chem. Chem. Phys., 15, 15371, https://doi.org/10.1039/c3cp50968k, 2013.

Varma, R. M., Venables, D. S., Ruth, A. A., Heitmann, U., Schlosser, E., and Dixneuf, S.: Long optical cavities for open-path monitoring of atmospheric trace gases and aerosol extinction, Appl. Opt., 48, B159–B171, https://doi.org/10.1364/ao.48.00b159, 2009.

Venables, D. S., Gherman, T., Orphal, J., Wenger, J. C., and Ruth, A. A.: High sensitivity in situ monitoring of $NO_3$ in an atmospheric simulation chamber using incoherent broadband cavity-enhanced absorption spectroscopy, Environ. Sci. Technol. , 40, 6758–6763, https://doi.org/10.1021/es061076j, 2006.

Vrekoussis, M., Kanakidou, M., Mihalopoulos, N., Crutzen, P. J., Lelieveld, J., Perner, D., Berresheim, H., and Baboukas, E.: Role of the $NO_3$ radicals in oxidation processes in the eastern Mediterranean troposphere during the MINOS campaign, Atmos. Chem. Phys., 4, 169–182, https://doi.org/10.5194/acp-4-169-2004, 2004.

Wagner, N. L., Dubé, W. P., Washenfelder, R. A., Young, C. J., Pollack, I. B., Ryerson, T. B., and Brown, S. S.: Diode laser-based cavity ring-down instrument for $NO_3$, $N_2O_5$, NO, $NO_2$ and $O_3$ from aircraft, Atmos. Meas. Tech., 4, 1227–1240, https://doi.org/10.5194/amt-4-1227-2011, 2011.

Wang, D., Hu, R. Z., Xie, P. H., Liu, J. G., Liu, W. Q., Qin, M., Ling, L. Y., Zeng, Y., Chen, H., Xing, X. B., Zhu, G. L., Wu, J., Duan, J., Lu, X., and Shen, L. L.: Diode laser cavity ring-down spectroscopy for in situ measurement of $NO_3$ radical in ambient air, J. Quant. Spectrosc. Radiat. Trans., 166, 23–29, https://doi.org/10.1016/j.jqsrt.2015.07.005, 2015.

Wang, H., Chen, J., and Lu, K.: Development of a portable cavity-enhanced absorption spectrometer for the measurement of ambient $NO_3$ and $N_2O_5$: experimental setup, lab characterizations, and field applications in a polluted urban environment, Atmos. Meas. Tech., 10, 1465–1479, https://doi.org/10.5194/amt-10-1465-2017, 2017.

Wang, H. and Lu, K.: Monitoring ambient nitrate radical by open-path cavity-enhanced absorption spectroscopy, Anal. Chem., 91, 10687–10693, https://doi.org/10.1021/acs.analchem.9b01971, 2019.

Wang, H., Chen, X., Lu, K., Hu, R., Li, Z., Wang, H., Ma, X., Yang, X., Chen, S., Dong, H., Liu, Y., Fang, X., Zeng, L., Hu, M., and Zhang, Y.: $NO_3$ and $N_2O_5$ chemistry at a suburban site during the EXPLORE-YRD campaign in 2018, Atmos. Environ., 224, 117180, https://doi.org/10.1016/j.atmosenv.2019.117180, 2020.

Wang, M., Varma, R., Venables, D. S., Zhou, W., and Chen, J.: A demonstration of broadband cavity-enhanced absorption spectroscopy at deep-ultraviolet wavelengths: Application to sensitive real-time detection of the aromatic pollutants benzene, toluene, and xylene, Anal. Chem., 94, 4286–4293, https://doi.org/10.1021/acs.analchem.1c04940, 2022.

Wang, S., Shi, C., Zhou, B., Zhao, H., Wang, Z., Yang, S., and Chen, L.: Observation of $NO_3$ radicals over

Shanghai, China, Atmos. Environ., 70, 401–409, https://doi.org/10.1016/j.atmosenv.2013.01.022, 2013.

Wang, X., Wang, T., Yan, C., Tham, Y. J., Xue, L., Xu, Z., and Zha, Q.: Large daytime signals of $N_2O_5$ and $NO_3$ inferred at 62 amu in a TD-CIMS: chemical interference or a real atmospheric phenomenon?, Atmos. Meas. Tech., 7, 1–12, https://doi.org/10.5194/amt-7-1-2014, 2014.

Washenfelder, R. A., Langford, A. O., Fuchs, H., and Brown, S. S.: Measurement of glyoxal using an incoherent broadband cavity enhanced absorption spectrometer, Atmos. Chem. Phys., 8, 7779–7793, https://doi.org/10.5194/acp-8-7779-2008, 2008.

Werle, P., MuCke, R., and Slemr, F.: The limits of signal averaging in atmospheric trace-gas monitoring by tunable diode-laser absorption spectroscopy (TDLAS), Appl. Phys. B-Photo., 57, 131–139, https://doi.org/10.1007/bf00425997, 1993.

Winer, A. M., Atkinson, R., and Pitts, J. N.: Gaseous nitrate radical: Possible nighttime atmospheric sink for biogenic organic compounds, Science, 224, 156–159, https://doi.org/10.1126/science.224.4645.156, 1984.

Wood, E. C., Wooldridge, P. J., Freese, J. H., Albrecht, T., and Cohen, R. C.: Prototype for in situ detection of atmospheric $NO_3$ and $N_2O_5$ via laser-induced fluorescence, Environ. Sci. Technol., 37, 5732–5738, https://doi.org/10.1021/es034507w, 2003.

Wu, H., Chen, J., Liu, A. W., Hu, S. M., and Zhang, J. S.: Cavity ring-down spectroscopy measurements of ambient $NO_3$ and $N_2O_5$ dagger, Chinese J. Chem. Phys., 33, 1–7, https://doi.org/10.1063/1674-0068/cjcp1910173, 2020.

Wu, T., Coeur-Tourneur, C., Dhont, G., Cassez, A., Fertein, E., He, X., and Chen, W.: Simultaneous monitoring of temporal profiles of $NO_3$, $NO_2$ and $O_3$ by incoherent broadband cavity enhanced absorption spectroscopy for atmospheric applications, J. Quant. Spectrosc. Radiat. Trans., 133, 199-205, https://doi.org/10.1016/j.jqsrt.2013.08.002, 2014.

Yokelson, R. J., Burkholder, J. B., Fox, R. W., Talukdar, R. K., and Ravishankara, A. R.: Temperature dependence of the $NO_3$ absorption spectrum, J. Phys. Chem., 98, 13144-13150, https://doi.org/10.1021/j100101a009, 1994.

Young, I. A. K., Murray, C., Blaum, C. M., Cox, R. A., Jones, R. L., and Pope, F. D.: Temperature dependent structured absorption spectra of molecular chlorine, Phys. Chem. Chem. Phys., 13, 15318, https://doi.org/10.1039/c1cp21337g, 2011.

Young, I. A. K., Jones, R. L., and Pope, F. D.: The UV and visible spectra of chlorine peroxide: Constraining the atmospheric photolysis rate, Geophys. Res. Lett., 41, 1781–1788, https://doi.org/10.1002/2013gl058626, 2014.

Zhou, W., Zhao, J., Ouyang, B., Mehra, A., Xu, W., Wang, Y., Bannan, T. J., Worrall, S. D., Priestley, M., Bacak, A., Chen, Q., Xie, C., Wang, Q., Wang, J., Du, W., Zhang, Y., Ge, X., Ye, P., Lee, J. D., Fu, P., Wang, Z., Worsnop, D., Jones, R., Percival, C. J., Coe, H., and Sun, Y.: Production of $N_2O_5$ and $ClNO_2$ in summer in urban Beijing, China, Atmos. Chem. Phys., 18, 11581–11597, https://doi.org/10.5194/acp-18-11581-2018, 2018.